

UKAEA-CCFE-PR(18)10

C. Bourdelle, Y. Camenen, J. Citrin, M. Marin,  
F. J. Casson, F. Koechl and M. Maslov

# **Fast H isotope and impurity mixing in Ion-Temperature- Gradient turbulence**

Enquiries about copyright and reproduction should in the first instance be addressed to the UKAEA Publications Officer, Culham Science Centre, Building K1/0/83 Abingdon, Oxfordshire, OX14 3DB, UK. The United Kingdom Atomic Energy Authority is the copyright holder.

# **Fast H isotope and impurity mixing in Ion-Temperature-Gradient turbulence**

C. Bourdelle,<sup>1</sup> Y. Camenen,<sup>2</sup> J. Citrin,<sup>3</sup> M. Marin,<sup>3</sup> F. J. Casson,<sup>4</sup>  
F. Koechl<sup>5</sup> and M. Maslov

<sup>1</sup>CEA, IRFM, F-13108 Saint-Paul-lez-Durance, France

<sup>2</sup>CNRS, Aix-Marseille Univ., PIIM UMR7345, Marseille, France

<sup>3</sup>DIFFER - Dutch Institute for Fundamental Energy Research, De Zaale 20, 5612 AJ Eindhoven, the Netherlands

<sup>4</sup>CCFE, Culham Science Centre, Abingdon, Oxon, OX14 3DB, UK

<sup>5</sup>ÖAW/ATI, Atominstitut, TU Wien, 1020 Vienna, Austria



# Fast H isotope and impurity mixing in Ion-Temperature-Gradient turbulence

C. Bourdelle<sup>1</sup>, Y. Camenen<sup>2</sup>, J. Citrin<sup>3</sup>, M. Marin<sup>3</sup>, F.J. Casson<sup>4</sup>, F. Koechl<sup>5</sup>, M. Maslov<sup>4</sup>

<sup>1</sup> CEA, IRFM, F-13108 Saint-Paul-lez-Durance, France

<sup>2</sup> CNRS, Aix-Marseille Univ., PIIM UMR7345, Marseille, France

<sup>3</sup> DIFFER - Dutch Institute for Fundamental Energy Research, De Zaale 20, 5612 AJ Eindhoven, the Netherlands

<sup>4</sup> CCFE, Culham Science Centre, Abingdon, Oxon, OX14 3DB, UK

<sup>5</sup> ÖAW/ATI, Atominstitut, TU Wien, 1020 Vienna, Austria

**Abstract.** In Ion-Temperature-Gradient (ITG) driven turbulence, the resonance condition leads to ion particle turbulent transport coefficients significantly larger than electron particle turbulent transport coefficients. This is shown in non-linear gyrokinetic simulations and explained by an analytical quasilinear model. It is then illustrated by JETTO-QuaLiKiz integrated modelling. Large ion particle transport implies that the ion density profiles are uncorrelated to the corresponding ion source, hence peaked isotope density profiles even in the absence of core source, no accumulation of He ashes and fast impurity transport. Furthermore, the relaxation time of the individual ion profiles in a mixed system can be significantly faster than the total density profile relaxation time which is constrained by the electrons. In Trapped-Electron-Mode (TEM) turbulence, in presence of electron heating about twice the ion heating, the situation is the inverse: ion particle turbulent transport coefficients are smaller than their electron counterpart.

## 1. Introduction

The amplitude of ion turbulent particle transport coefficients with respect to electron turbulent particle transport coefficients has significant consequences in multiple-ion plasmas. Despite the ambipolarity of the particle fluxes, the diffusive and convective ion coefficients are significantly larger from those of electrons in ion-temperature-gradient (ITG) driven turbulence. Therefore, for multiple ion plasma, the ion density profiles are less sensitive to the ion particle sources. This leads to fast isotope mixing, no core He ash accumulation, and fast impurity transport.

In a single-ion plasma, the ambipolarity constraint is cast as follows.

$$\Gamma_e = Z_i \Gamma_i \quad (1)$$

Where  $\Gamma$  is the particle flux, and  $Z_i$  the ion charge number. The particle fluxes are decomposed into diffusive and convective components:

$$\Gamma_e = -D_e \frac{\partial n_e}{\partial r} + V_e n_e \quad (2)$$

$$\Gamma_i = -D_i \frac{\partial n_i}{\partial r} + V_i n_i \quad (3)$$

Even if  $D_i \gg D_e$  and  $|V_i| \gg |V_e|$ , ambipolarity can still be respected, for example by a large outward ion diffusion counterbalanced by a large ion inward convective velocity (pinch). In this case, time-scale for relaxation of the core density profile (identical for ions and electrons) is set by the slower dynamics of the electrons.

However, in multiple ion plasmas, there is more freedom in the ambipolarity constraint:

$$\Gamma_e = \sum_i Z_i \Gamma_i \quad (4)$$

In this case, the individual ion fluxes are not tied to the electron flux. Ion density profile transients can thus relax at a different timescale to the electron particle confinement time. As will be shown for ITG turbulence, these transients can relax at timescales comparable to the energy confinement time, owing to the large  $D_i$  and  $V_i$ . Furthermore, these large ion transport coefficients reduce the dependence of the individual ion density profiles on the core sources, since any unbalanced density gradient leads to large fluxes that dominate the source term, as seen in the density transport equation:

$$\frac{\partial n_i}{\partial t} = -\frac{1}{V'} \frac{\partial}{\partial r} (V' \Gamma_i) + S_i \quad (5)$$

where  $S_i$  is the source term and  $V'$  the radial derivative of the plasma volume, which in stationary state implies:

$$-\frac{1}{n_i} \frac{\partial n_i}{\partial r} = -\frac{V_i}{D_i} + \frac{1}{V'} \int_0^r V' \frac{S_i}{n_i D_i} dr \quad (6)$$

These statements are supported in this paper through nonlinear simulations, analytical derivations and quasilinear transport models both in standalone mode and used in conjunction with an integrated modelling suite.

Moreover, experimental evidence for fast isotope mixing has already been seen. In trace tritium (T) experiments on TFTR [1], where tritium gas were puffed into deuterium neutral-beam fueled plasmas, the T profile peaked over 100 ms, significantly faster than the energy confinement time of 160 ms. In similar trace T at JET, the T profile is also observed to peak in the center with ratios of  $D_T/\chi_{\text{eff}}$  varying between 0.3 and 2 [2]. Recent analysis of JET mixed isotope (H/D) experiments has shown that the density peaking of H and D isotopes are similar, and independent of the relative location of H and D core and edge sources, both with D pellet in H plasmas [3] and in D puff in H plasmas [4]. In this latest case,  $D$  of H and D are up to  $3 \times \chi_{\text{eff}}$  [4].

Concerning trace helium (He) gas puff in D plasmas on DIII-D, it was found that, after 200 ms, the He density profile was similar to the electron density profiles for various scenarios (L and H modes). The fast He core transport led to the conclusion that He ash removal is limited only by the recycling and pumping regime [5]. This conclusion is supported by linear and nonlinear gyrokinetic simulations, together with integrated modelling using a quasilinear transport model [6] where He diffusivities ( $D_{He}$ ) of the order of the effective heat diffusivities  $\chi_{\text{eff}}$  are found. In further gyrokinetic nonlinear simulations of mixed D-He plasma [7], significant  $D_{He}/\chi_{\text{eff}}$  ratios were observed for a range of He normalized density gradients, hinting at fast relaxation times for He transients, although this was not specifically discussed.

Concerning impurity transport, Si laser-blow-off experiments at AUG [8, 9] showed large anomalous impurity diffusion coefficients, with  $D_{Si} \geq \chi_{\text{eff}}$ , extending inwards to the plasma centre with on-axis electron heating. Further laser-blow-off experiments at JET, Tore-Supra and CMOD also measured short impurity confinement times, significantly lower than

the energy confinement time [10, ?].

Significant dependence of impurity transport to the ion to electron heat flux ratio (and hence turbulence regime) has been predicted [11, 12, 6, 13, 14] by nonlinear and quasilinear gyrokinetic simulations.

However, to our knowledge, the ratios of ion to electron diffusivity and convectivity,  $D_i/D_e$  and  $|V_i|/|V_e|$ , and their dependence on turbulence regime, has never been pointed out. The novelty of this paper then lies in the following: i) the prediction of separate particle confinement timescales for electrons and ions, which then is only evident for either impurities or multi-isotope plasmas; ii) integrated modelling simulations of multiple-isotope plasmas with a first-principle-based gyrokinetic turbulent transport model, with positive ramifications for isotope mixing.

In section 2, the dependence of  $D_i/D_e$  and  $|V_i|/|V_e|$  on turbulence regime is shown in nonlinear gyrokinetic simulations performed by GKW [15]. In section 3, using the quasilinear gyrokinetic derivation of turbulent fluxes [16], we explain why larger ion transport coefficients than electron transport coefficients are expected in the case of dominant ITG background turbulence, while the inverse holds for Trapped Electron Mode (TEM) turbulence. In section 4, the trends observed in the nonlinear simulations are replicated by quasilinear calculations using the QuaLiKiz transport model [16, 17], and further dependencies are explored. Finally in section 5, integrated modelling using QuaLiKiz within the JETTO integrated modelling suite [18, 19] is used to directly simulate the behaviour and timescales of multiple-ion particle transport.

## 2. Ion to electron particle diffusivity and convection in nonlinear GKW simulations

The ion and electron particle transport coefficients predicted by non-linear gyrokinetic simulations is compared for two reference cases. The first one is the GA standard case [20] and is dominated by ITG turbulence, see Table 1. A second reference case dominated by TEM turbulence is obtained by setting the logarithmic ion temperature gradient  $R/L_{T_i}$  to zero in the GA standard case, cf Table 1. The simulations are performed with the non-linear gyrokinetic code GKW [15] in its flux-tube mode (local approximation). To compute the ion and electron particle diffusivity and pinch, four kinetic species are included in the simulation: two main species, deuterium and electrons, and two trace species with zero density gradient but otherwise identical to the main species. Alternatively (and equivalently), four non-trace species could be used provided their respective density gradient combine to a total of  $R/L_n = 3$  for each species. The actual electron

to deuterium mass ratio is used. The logarithmic ion temperature gradient is  $R/L_{T_i} = 9$  for the first case (ITG1) and  $R/L_{T_i} = 0$  for the second case (TEM1). No collisions, or rotation physics are included. The magnetic equilibrium is prescribed using the Miller parametrisation [21] for a circular plasma cross-section. The input parameters for the ITG1 and TEM1 cases are summarized in Table 1.

Case	$\frac{r}{R_0}$	$q$	$\hat{s}$	$\frac{R}{L_{T_e}}$	$\frac{R}{L_{n_e}}$	$\frac{R}{L_{T_i}}$	$\frac{R}{L_{n_i}}$	$\frac{T_e}{T_i}$
ITG1	0.1667	2	1	9	3	9	3	1
TEM1	0.1667	2	1	9	3	0	3	1

**Table 1.** Summary of the input parameters (main species only) for the ITG1 and TEM1 cases.

The 5D computational domain is discretised with  $N_s = 32$  points in the direction parallel to the magnetic field (finite differences),  $N_{k_\theta} \times N_{k_r} = 21 \times 339$  in the perpendicular plane (spectral decomposition) and  $N_\mu \times N_{v_\parallel} = 16 \times 48$  points in velocity space (finite differences). The poloidal wave vectors range from  $k_\theta \rho_i = 0$  to 1.2, with  $\rho_i$  the ion Larmor radius at the thermal velocity  $v_{\text{thi}} = \sqrt{2T_i/m_i}$  and the radial wave vectors from  $k_r \rho_i = -10.73$  to 10.73.

The temporal evolution of the electron and ion heat fluxes is shown in the top row of Fig. 1. As expected, the electron heat flux is larger than the ion heat flux for the TEM dominated case, whereas the opposite is observed for the ITG dominated case. The particle diffusivities,  $D_e$  and  $D_i$ , and pinches,  $V_e$  and  $V_i$ , defined in Eqs. (2-3) are computed by combining the main species and trace particle fluxes:

$$D_s = \frac{1}{R/L_{n_s}} \left[ \frac{R_0 \Gamma_s^{\text{main}}}{n_s^{\text{main}}} - \frac{R_0 \Gamma_s^{\text{trace}}}{n_s^{\text{trace}}} \right] \quad (7)$$

$$V_s = \frac{\Gamma_s^{\text{trace}}}{n_s^{\text{trace}}} \quad (8)$$

where the subscript  $s$  represents the species label ( $e$  or  $i$ ). Note that the values of  $D_s$  and  $V_s$  are “local” values in the sense that, for the main species, they depend on  $R/L_{n_s}$  (i.e.  $\Gamma_s$  is not linear in  $R/L_{n_s}$ ). The temporal evolution of the particle transport coefficients is shown in the bottom row of Fig. 1. Interestingly, for the TEM dominated case  $D_e > D_i$  and  $|V_e| > |V_i|$  whereas the opposite is found for the ITG dominated case ( $D_i > D_e$  and  $|V_i| > |V_e|$ ), see also Table 2. As highlighted in the introduction, this difference in the electron and ion transport coefficients does not prevent the intrinsic ambipolarity of the particle fluxes ( $\Gamma_e = \Gamma_i = 4.7569 n T \rho_*^2 v_{\text{thi}}$  for the TEM1 case and  $\Gamma_e = \Gamma_i = -0.0366 n T \rho_*^2 v_{\text{thi}}$  for the ITG1 case) It has, however, important consequences for the response of the density profile to a core particle source or sink that will be discussed in Section 5 thanks to flux driven integrated modeling. In Table 2, the time average is

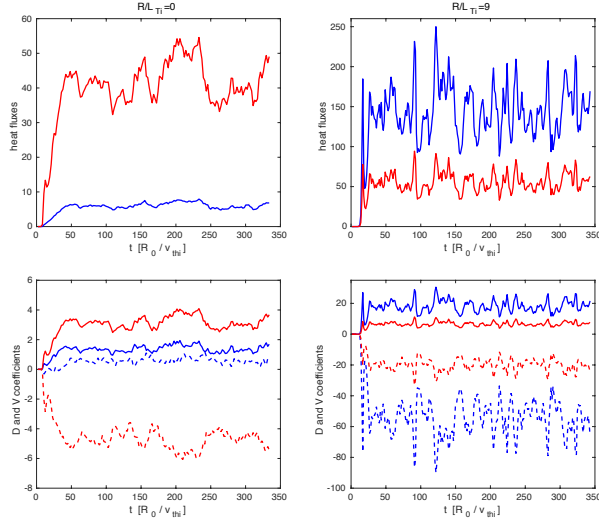


**Figure 1.** Top row: time evolution of the electron (red) and ion (blue) heat fluxes in the non-linear simulations at  $R/L_{Ti} = 0$  (left column) and  $R/L_{Ti} = 9$  (right column). Bottom row: corresponding particle diffusivity (full lines,  $D_e$  in red and  $D_i$  in blue) and particle pinch (dashed lines,  $V_e$  in red and  $V_i$  in blue). The heat fluxes are normalised to  $nT\rho_*^2v_{thi}$ , the diffusivities to  $\rho_*^2v_{thi}R_0$  and the pinch coefficients to  $\rho_*^2v_{thi}$ .

performed from  $t = 60R_0/v_{thi}$  to  $t = 300R_0/v_{thi}$  and gyro-Bohm normalisation is used with  $\rho_* = \rho_i/R_0$ . The effective heat diffusivity is defined as  $Q_e + Q_i = -n_e\chi_{eff}(\partial T_e/\partial r + \partial T_i/\partial r)$ . As seen in 2, for ITG1  $D_i > \chi_{eff} > D_e$ , for TEM1  $D_i < D_e < \chi_{eff}$ . In

$R/L_{Ti}$	$Q_e$	$Q_i$	$\chi_{eff}$	$D_e$	$D_i$	$V_e$	$V_i$
0	42.0	6.1	5.3	3.2	1.4	-4.7	0.6
9	55.7	145.5	11.2	6.7	18.3	-20.0	-54.8

**Table 2.** Time averaged values of the electron and ion heat flux, particle diffusivity and particle pinch obtained in the non-linear simulations at  $R/L_{Ti} = 0$  and  $R/L_{Ti} = 9$  (GA standard case). The heat fluxes are normalised to  $nT\rho_*^2v_{thi}$ , the diffusivities to  $\rho_*^2v_{thi}R_0$  and the pinch coefficients to  $\rho_*^2v_{thi}$ .

the following section, a quasilinear derivation of the particle fluxes will explain why the ratio of  $D_i/D_e$  is larger in ITG dominated regime than in TEM dominated regime.

### 3. Quasilinear derivation of ion to electron particle transport coefficients

In this section, analytical expressions for the ion to electron particle transport coefficient are derived based on the quasilinear flux formulation, with additional approximations to allow focusing on the essential physics that sets the ion to electron  $D$  and  $V$  ratios.

The quasilinear approach and justifications thereof are summarized in Refs.[22, 23, 24, 25, 17] and

references therein. The quasilinear particle flux is defined as  $\Gamma_s = \langle \delta n_s \delta V_{E \times B} \rangle$ , where  $\langle \dots \rangle$  is a flux surface average and time average over  $\tau$ , an intermediate timescale  $1/\gamma < \tau < T_0$ , where  $T_0$  is the equilibrium (transport) timescale and  $\gamma$  the linear growth rate. For electrostatic turbulence using the linearized Vlasov equation, the particle flux for a given mode  $k$  can be expressed as the product of a linear plasma response with a saturated electrostatic potential as follows:

$$\begin{aligned} \Gamma_{ks} &= \text{Re} \langle \delta n_s \frac{ik_\theta \delta \phi}{B} \rangle \\ &\simeq - \langle k_\theta \frac{f_0^s e_s}{BT_s} \text{Im} \frac{n\omega_s^* - n\omega_{ds} - k_\parallel v_{\parallel,s}}{\omega_k - n\omega_{ds} - k_\parallel v_{\parallel,s} + i0^+} |\phi_k|^2 \rangle_{\epsilon, \lambda, \theta} \end{aligned} \quad (9)$$

where the integration is over velocity space (energy and pitch angle) and flux surface.  $\omega_k$  is the real part of the eigenfrequency calculated from the dispersion relation defined by the weak formulation of the quasineutrality constraint  $\langle \sum_s q_s \delta n_s \phi_k \rangle = 0$ . This constraint also ensures intrinsic ambipolarity for each mode, as defined by  $\sum_i Z_i \Gamma_{ki} = \Gamma_{ke}$ .  $n\omega_{ds}$  is the  $\nabla B$  and curvature drift:

$$n\omega_{ds} \simeq - \frac{k_\theta T_s}{e_s B R} \mathcal{E} (2 - \lambda b(\theta)) \quad (10)$$

where  $e_s$  is the species charge,  $B$  the magnetic field,  $R$  the major radius,  $\lambda$  is the pitch angle at the low-field-side (LFS), and  $b(\theta)$  the poloidally dependent modification of the pitch angle due to the magnetic mirror effect.  $\mathcal{E}$  is the particle energy normalised to the species temperature. The parallel dynamics term is:

$$k_\parallel v_{\parallel,s} \simeq k_\theta x \frac{\hat{s}}{q} \frac{v_{ths}}{R} \sqrt{\mathcal{E}} \quad (11)$$

Where  $q$  is the safety factor,  $\hat{s}$  the magnetic shear,  $x$  is the distance from the central flux surface of the mode, and  $v_{ths} \equiv \sqrt{2T_s/m_s}$  the thermal velocity. The diamagnetic frequency  $n\omega_s^*$  due to gradients with respect to the equilibrium Maxwellian  $f_0$  is:

$$n\omega_s^* = -k_\theta \frac{T_s}{e_s B R} \left( \frac{R}{L_{ns}} + \left( \mathcal{E} - \frac{3}{2} \right) \frac{R}{L_{Ts}} \right) \quad (12)$$

where we have ignored rotation effects, and  $L_{ns} \equiv -\frac{\nabla n_s}{n_s}$ ,  $L_{Ts} \equiv -\frac{\nabla T_s}{T_s}$ . We have defined the negative direction as the ion diamagnetic direction.

Nonlinear effects broaden the frequency spectrum, hence a finite value will be used instead of  $0^+$  in Eq. (9). It has been shown that for low- $k$  modes which drive the majority of the transport, the frequency spectrum can be represented by a Lorentzian whose width is of the order of  $\gamma_k$ , the imaginary part of the solution of the dispersion relation (i.e. the growth



rate). This assumption has been shown to be valid over a large range of parameters [23, 25], and we apply it here henceforth. Note that energy, and momentum transport fluxes are similarly derived [26, 27].

We now make the following significant approximations to reduce Eq. (9) into an easily calculable form maintaining the key physics setting the  $D_i/D_e$  and  $V_i/V_e$  ratios.

- Remove spatial dependence by focusing on the outboard midplane and setting  $\theta = 0$ . Hence  $b(\theta) = 0$  in Eq. (10), and  $\phi_k$  becomes a scalar. We also set an average  $x \approx d$ , where  $d = 1/\hat{s}k_\theta$  is the distance between neighbouring flux surfaces. This sets  $k_\parallel \approx 1/qR$
- Simplify the velocity space integration by assuming all passing particles have pitch angle  $\lambda = 0$ , and all trapped particles have  $\lambda = 1$ . The pitch angle integration then simply extracts the trapped and passing particle fractions
- Bounce average the trapped particles, which then removes the parallel dynamics term for trapped particles (on average  $v_\parallel = 0$ )
- Neglect impact of collisions on the quasilinear response, and assume  $T_s = T$  for all particle species
- Take a drift kinetic limit and neglect finite Larmor radius effects

Following these approximations, we can split the contribution of the particle flux of each species, for a given mode  $k$ , by trapped  $\Gamma_{ts}$  and passing particles  $\Gamma_{ps}$ , as follows:

$$\Gamma_{ts} \propto f_t \left\langle \frac{\frac{R}{L_{n_s}} + (v^2 - \frac{3}{2}) \frac{R}{L_{T_s}} - v^2}{\left(\bar{\omega}_k + \frac{k_\theta \rho_0}{Z_s} v^2\right)^2 + \bar{\gamma}_k^2} \right\rangle \quad (13)$$

$$\Gamma_{ps} \propto f_p \left\langle \frac{\frac{R}{L_{n_s}} + (v^2 - \frac{3}{2}) \frac{R}{L_{T_s}} - 2v^2 + \frac{Z_s}{q} \sqrt{\frac{2m_p}{m_s}} \frac{v}{k_\theta \rho_0}}{\left(\bar{\omega}_k + \frac{2k_\theta \rho_0}{Z_s} v^2 - \frac{1}{q} \sqrt{\frac{2m_p}{m_s}} v\right)^2 + \bar{\gamma}_k^2} \right\rangle \quad (14)$$

where  $v^2 \equiv \mathcal{E}$ ,  $f_{t,p}$  are the trapped and passing fractions respectively, and  $\langle \cdot \rangle$  here represents integration over  $v$ :  $\int_{-\infty}^{\infty} v^2 e^{-v^2} dv$ . Both  $\Gamma_t$  and  $\Gamma_p$  share the same proportionality constant.  $\rho_0 \equiv \frac{\sqrt{T m_p}}{e B}$  is the Larmor radius with respect to the proton sound speed  $c_s = \sqrt{T/m_p}$ , where  $m_p$  is the proton mass.  $\bar{\omega}_k$  and  $\bar{\gamma}_k$  correspond to normalization by  $c_s/R$ .

### 3.1. The quasilinear ratio of ion to electron transport coefficients

The particle flux  $\Gamma_s$  can be decomposed as:

$$\Gamma_s = -D_s \frac{dn_s}{dr} + (V_{t,s} + V_{c,s}) n_s \quad (15)$$

where we neglect rotation. For a review on particle transport and the various convective terms see [28, 29].  $D_s$  is the diffusion term,  $V_{t,s}$  is the thermodiffusion convective velocity, and  $V_{c,s}$  is the pure convective velocity. From Eqs (13-14), it is clear that  $D$  arises from the term proportional to  $\frac{R}{L_n}$  in  $n\omega_s^*$ ,  $V_t$  from the term proportional to  $\frac{R}{L_T}$  in  $n\omega_s^*$ , and  $V_c$  from the terms proportional to the  $\nabla B$  drift frequency and parallel dynamics term.

We now directly calculate, for a single mode,  $D_i/D_e$ .

$$\begin{aligned} \frac{D_i}{D_e} &= \frac{D_{ip} + D_{it}}{D_{ep} + D_{et}} \\ &= \frac{\left\langle \frac{f_p}{\left(\bar{\omega}_k + \frac{2k_\theta \rho_0}{Z_i} v^2 - \frac{1}{q} \sqrt{\frac{2m_p}{m_i}} v\right)^2 + \bar{\gamma}_k^2} + \frac{f_t}{\left(\bar{\omega}_k + \frac{k_\theta \rho_0}{Z_i} v^2\right)^2 + \bar{\gamma}_k^2} \right\rangle}{\left\langle \frac{f_p}{\left(\bar{\omega}_k - 2k_\theta \rho_0 v^2 - \frac{1}{q} \sqrt{\frac{2m_p}{m_e}} v\right)^2 + \bar{\gamma}_k^2} + \frac{f_t}{(\bar{\omega}_k - k_\theta \rho_0 v^2)^2 + \bar{\gamma}_k^2} \right\rangle} \end{aligned} \quad (16)$$

For the trapped particles, a resonance in the Lorentzian leading to large diffusivities, is only possible for modes drifting in the ion diamagnetic direction,  $\bar{\omega}_k < 0$ , for  $D_{it}$  and for modes drifting in the electron diamagnetic direction,  $\bar{\omega}_k > 0$ , for  $D_{et}$ . Concerning passing particles, the  $\sqrt{m_p/m_e}$  in the electron parallel dynamics term means that only a narrow resonance occurs, such that the contribution of  $D_{ep}$  to  $D_e$  is negligible. We thus expect that  $D_i/D_e > 1$  for Ion Temperature Gradient (ITG) modes with  $\omega_k < 0$ , and  $D_i/D_e < 1$  for Trapped Electron Modes (TEM) with  $\omega_k > 0$ , as observed in the GKW nonlinear simulations, Fig. 1. The present analytical derivation, Eq. (16), is illustrated in Fig. 2, with  $A_i = 2$  and  $Z_i = 1$ . The calculation is performed for a typical growth rate value of  $\bar{\gamma} = 0.2$ ,  $f_p = f_t$ , a typical ion-scale mode wavevector of  $k_\theta \rho_0 = 0.5$ , and  $q = 2$ .  $\bar{\omega}_k$  was scanned in both ion and electron diamagnetic directions. While we have not calculated the precise eigenvalue, the general dependence of  $D_i/D_e$  on the turbulence regime is robust against the exact location of the eigenvalue. Note that the  $D_i/D_e = 1$  location is not at  $\bar{\omega}_k = 0$  due to non-negligible contributions of the passing ion flux in the  $\bar{\omega}_k > 0$  region. This points to TEM modes having  $D_i/D_e$  closer to unity than in ITG modes, a

trend already evident in the nonlinear simulations in Section 2, Fig. 1.

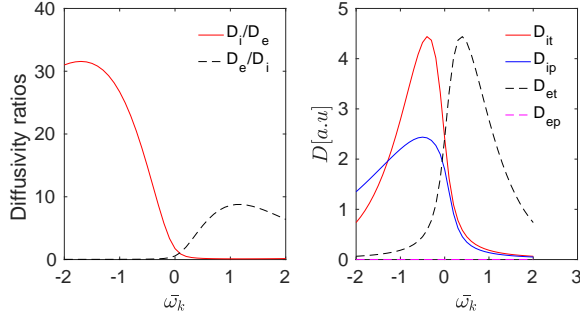


**Figure 2.** Ratios of  $D_i/D_e$  and  $D_e/D_i$  for a range of input frequencies (left panel), corresponding to a direct calculation of Eq. 16, with  $\bar{\gamma} = 0.2$ . The right panel shows the breakdown of the contribution to the diffusivities according to trapped and passing ions, and trapped and passing electrons. Note that the passing electron contribution is always negligible.

This dependence of  $D_i/D_e$  on the resonance condition is strongly related to the well known result that ion heat flux dominates electron heat flux for ITG dominated regimes, and electron heat flux is dominant for TEM regimes. Therefore the parametric dependencies of  $D_i/D_e$  are expected to be similar to the one of  $Q_i/Q_e$ . Note that this does not hold for angular momentum, where the electron to ion mass ratio leads to negligible electron angular momentum independently of the turbulence nature.

Concerning the convection velocity ratios, integrations similar to Eq. (16) for the thermodiffusion ratio  $V_{t,i}/V_{t,e}$  and the pure convective ratio  $V_{c,i}/V_{c,e}$  are carried out. In spite of the modified  $v$  dependences, one finds, as illustrated on Fig. 3, that both  $|V_{t,i}/V_{t,e}|$  and  $V_{c,i}/V_{c,e}$  share the same trend as  $D_i/D_e$ :  $> 1$  for ion modes and  $< 1$  for electron modes. We note that  $V_{t,i}/V_{t,e}$  has lower absolute values compared to the other ratios, particularly in the range  $\bar{\omega}_k < 1$ .  $V_{t,i}/V_{t,e}$  can also change sign, likely due to the  $v^2 - \frac{3}{2}$  dependence in the numerator, and the dependence of the  $v$  resonance location on  $\bar{\omega}_k$ .

Finally, we discuss the mass and charge dependence of the  $D_i/D_e$  ratio. For  $A_i$ , the only dependence is a  $\sqrt{A_i}$  dependence in the parallel dynamics term for the passing ions only, and hence the impact is expected to be weak. For ion (resp. electron) modes, higher  $Z_i$  narrows the width of the resonance, reducing the ion (resp. electron) particle diffusivity, see Eq. (16). We thus expect higher  $Z_i$  to decrease  $D_i/D_e$  for ion modes and to decrease  $D_e/D_i$  for electron modes. This is indeed observed in direct calculation (at  $\bar{\omega}_k = \pm 1$ ), displayed in Fig. 4 and summarized in Table 3. Note that while there is significant variation, the diffusivity ratio saturates at still high  $D_i/D_e$  at high  $Z_i$  for  $\bar{\omega} = -1$ .

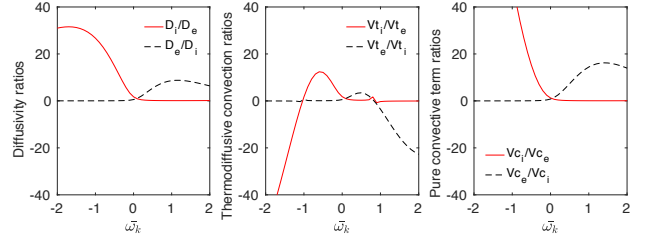


**Figure 3.** Left panel: Ratios of  $D_i/D_e$  and  $D_e/D_i$  for a range of input frequencies as in Fig. 2. Central panel: Ratios of  $V_{t,i}/V_{t,e}$  and  $V_{t,e}/V_{t,i}$  for a range of input frequencies. Right panel: Ratios of  $V_{c,i}/V_{c,e}$  and  $V_{c,e}/V_{c,i}$  for a range of input frequencies.

This indicates that we may expect fast impurity transport in the ITG regime.

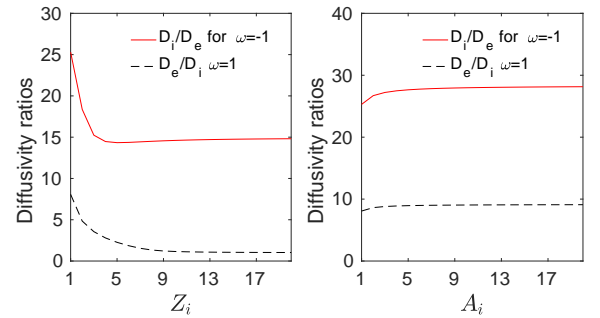


**Figure 4.** Ratio of  $D_i/D_e$  for a frequency in the ion diamagnetic direction ( $\bar{\omega}_k < 0$ ), and  $D_e/D_i$  for a frequency in the electron direction ( $\bar{\omega}_k > 0$ ), for a scan of ion charge (left panel) and ion mass (right panel).

	ITG dominated	TEM dominated
$D_i/D_e$	$> 1$	$< 1$
larger $Z_i$	$D_i/D_e$ decreases, then saturates at $D_i/D_e \gg 1$	$D_i/D_e$ increases, then saturates at $D_i/D_e \sim 1$
larger $A_i$	weak impact on $D_i/D_e$	weak impact on $D_i/D_e$

**Table 3.** Impact of turbulence nature,  $Z_i$ ,  $A_i$  on  $D_i/D_e$

#### 4. Parametric dependences of the ion to electron particle fluxes ratio in quasilinear QuaLiKiz simulations

Here we will focus on the particle transport fluxes using standalone QuaLiKiz. Situations where the dominant unstable modes are in the ion drift direction and in the electron direction are explored. The trend predicted in the previous section are recovered, the impact of the main ion mass/charge is explored as well as trace

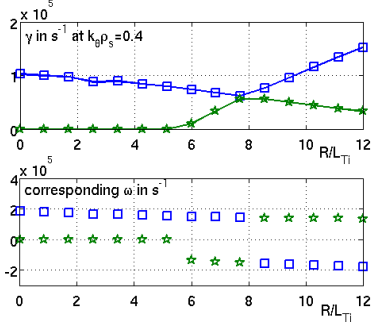


**Figure 5.** Upper figure: growth rate at  $k_{\theta}\rho_s = 0.4$  for the two most unstable branches versus  $R/L_{T_i}$  (other parameters from GA standard case, see Table 1). Lower figure: corresponding frequency versus  $R/L_{T_i}$ , when negative (resp. positive) the mode drifts in the ion (resp. electron) diamagnetic direction. Blue squares stand for the most unstable branch, green stars for the subdominant branch.

impurity transport dependences.

QuaLiKiz is run in stand-alone using 20 modes between  $k_{\theta}\rho_s = 0.1$  and 2. The relative accuracy on 1D and 2D integrals is  $10^{-4}$  and  $2 \times 10^{-3}$ , respectively.

#### 4.1. Impact of the turbulence regime on the particle fluxes ratio

The normalized ion temperature gradient  $R/L_{T_i}$  is scanned from 0 to 12, while the other parameters are the ones of the GA standard case, see Table 1, i.e. without collisions and without rotation. For  $R/L_{T_i} < 5$ , only modes drifting in the electron diamagnetic direction (positive frequency in QuaLiKiz normalizations) are unstable, see figure 5. As expected, for this TEM dominated regime, the ratio  $D_i/D_e$  stands well below one, see Fig. 6. For  $5 < R/L_{T_i} < 9$ , two unstable modes are co-existing, one in the ion drift direction (negative frequency) and one in the electron drift direction (positive frequency), see Fig. 5. In this region, although the most unstable mode is drifting in the electron drift direction, the destabilization of the ITG branch leads nonetheless to larger  $D_i/D_e$  as visible in Fig. 6. Finally, for  $R/L_{T_i} > 9$ , the ITG branch becomes dominant and the ratio  $D_i/D_e$  saturates to values much larger than unity, as expected.

The  $D_i/D_e$  ratios obtained in non-linear GKW simulations (see section 2) for the TEM1 case at  $R/L_{T_i} = 0$  and the ITG1 case at  $R/L_{T_i} = 9$  are added on figure 6. The quasi-linear estimates are very close to the non-linear values for these two cases.

The convection velocities are also plotted with respect to  $R/L_{T_i}$ . The overall trend for the total convective velocity ratio is similar to that of  $D_i/D_e$ , i.e. from below one in the TEM dominated regime to above one in the ITG dominated regime, see Fig. 7. Moreover, it is interesting to note that, as predicted by the analytical

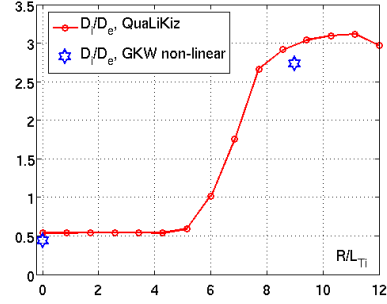


**Figure 6.** Ratio of electron to ion particle diffusivities versus  $R/L_{T_i}$  (other parameters from GA standard case, see Table 1). The red circles are for QuaLiKiz ratios and the blue stars for GKW ratios as given in Table 2.

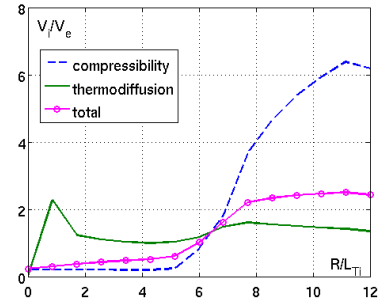


**Figure 7.** Ratio of electron to ion convective velocities, versus  $R/L_{T_i}$  (other parameters from GA standard case, see Table 1). Magenta circles: ratio of the total convective velocities. Blue dashed lines: ratio of the compressibility components. Green full lines: ratio of the thermodiffusion components.

model (see Fig. 3), the thermodiffusion ratio  $V_{t,i}/V_{t,e}$  has a weaker variation than the pure convective velocities ratio  $V_{c,i}/V_{c,e}$  over the  $R/L_{T_i}$  scan, see Fig. 7.

It is also interesting to note that the  $D_i/D_e$  ratio and the  $V_i/V_e$  ratio are strongly correlated to the ion to electron heat flux ratio, see Fig. 8. In particular,  $D_i/D_e$  is above one for  $Q_e < 2Q_i$ , on ion-scales, which is the case of most plasmas, including reactor-relevant alpha heated scenarios, where ion-electron heat exchange and radiation contribute to maintaining the heat flux ratio in an ITG regime [30, 31].

When comparing the diffusive and convective contributions to the ion particle flux (respectively  $D_i$  and  $RV_i$ ) to the total effective heat diffusivity  $\chi_{\text{eff}} = -\frac{Q_i + Q_e}{n_e \nabla T_e + n_i \nabla T_i}$  as often done in other modelling works [7, 6], one sees that it is mostly the convective contribution to the ion particle transport which is much larger than  $\chi_{\text{eff}}$  in the ITG dominated regime, with an inward  $RV_i$  up to 8 times  $\chi_{\text{eff}}$ , while  $D_i$  is at most 2.5 times larger than  $\chi_{\text{eff}}$ , Fig. 9. In the next section, these ratio will be compared to the ratio of the energy confinement time to the trace ion particle confinement time obtained within the integrated mod-

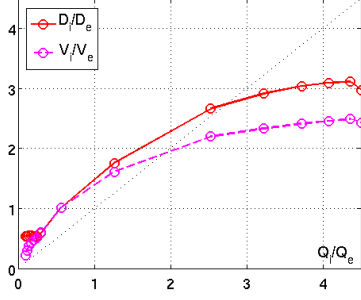


**Figure 8.** Ratio of electron to ion diffusivities and convective velocities versus  $Q_i/Q_e$  (other parameters from GA standard case, see Table 1). Magenta dashed line circles: ratio of the total convective velocities. Red line and circles: ratio of the diffusivities.

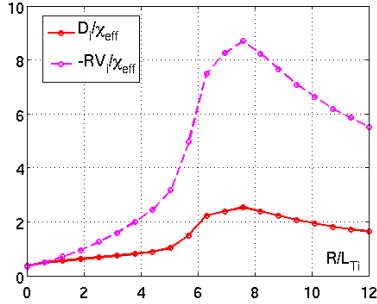


**Figure 9.** Ratio of the ion diffusivity and convective terms to  $\chi_{eff}$ , versus  $R/L_{Ti}$  (other parameters from GA standard case, see Table 1).

elling framework using QuaLiKiz-JETTO. So far we have considered collisionless plasmas. The  $D_i/D_e$  ratio with collisions is compared to the collisionless case in Fig. 10. The collisionality is calculated assuming  $T_e = T_i = 8\text{keV}$ ,  $n_e = n_i = 5 \times 10^{19}\text{m}^{-3}$ . As expected, with collisions, the TEM region in terms of  $R/L_{Ti}$  range is reduced and the ITG dominated regime takes over at lower values of  $R/L_{Ti}$ , leading to  $D_i/D_e$  above unity for lower  $R/L_{Ti}$  values. Moreover, the electron-ion collisionality  $\nu_{ei}/v^3$  added to  $\gamma_k$  in equation 16 on the trapped electron contribution, leads to larger  $D_i/D_e$  in the ITG dominated regime.

#### 4.2. Impact of the ion mass and charge on the ratio of ion to electron particle transport

The impact of the ion charge and mass is now investigated in the collisionless case. The weak dependence of  $D_i/D_e$  on the ion mass predicted by the analytical model of section 3 is confirmed in QuaLiKiz simulations for H, D and T, Fig. 11. On the contrary, the charge has a strong impact: in the ITG dominated regime  $D_i/D_e$  is reduced and in the TEM dominated

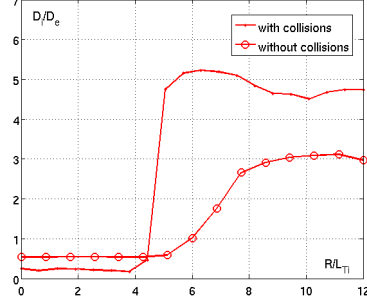


**Figure 10.** Ratio of electron to ion diffusivities, versus  $R/L_{Ti}$  (other parameters from GA standard case, see Table 1). Red line and circles: collisionless case. Red line and dots: collisional case.

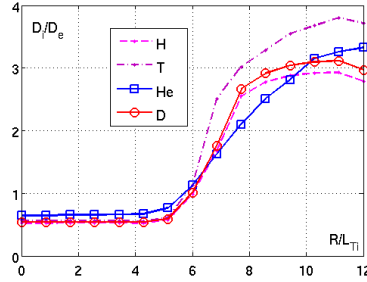


**Figure 11.** Ratio of electron to ion diffusivities, versus  $R/L_{Ti}$  for H, D, T and He without collisions (other parameters from GA standard case, see Table 1). Magenta dashed line and smaller circles: H. Red line and circles: D. Darker red dot-dashed line and smaller circles: T. Blue line and squares: He.

regime  $D_i/D_e$  is increased as observed when comparing D with He in Fig. 11.

Concerning trace impurities, a concentration of  $10^{-5}$  is assumed for the various species tested: W with a mass of 184 and charge states from 0 to 40, Ne A=20 Z=10, Ni A=56 Z=28 and Kr A=78 Z=36. The various impurities are illustrated on figure 12 for the ITG dominated case and figure 13 for the TEM dominated case. The W various ionisation states are plotted with full lines, Ne with diamonds, Ni with circles and Kr with squares. As for the main ions, the mass variation does not lead to significant differences. Indeed, for both ITG and TEM dominated regimes, the ratio of the trace impurity diffusivity to the electron diffusivity,  $D_Z/D_e$ , is only weakly affected by a mass change from 184 for W to 10 for Ni. On the contrary the charge of the trace impurity does matter, leading to larger  $D_Z/D_e$  for larger charges in both regimes as illustrated on figures 12 and 13. As for main ions, larger  $D_Z/D_e$  ratios are observed in the ITG dominated regime, while  $D_Z/D_e$  remains lower than unity for the TEM dominated case. In

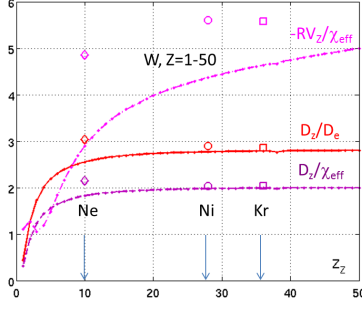


**Figure 12.** Ratio between the trace impurity diffusivity and  $1/\text{the electron diffusivity}$  (red)  $2/\text{the effective heat diffusivity}$  (purple), ratio between the  $-R\times$  the trace impurity convective velocity (magenta) and the effective heat diffusivity versus  $Z_z$ , for the ITG1 case (see Table 1). For  $A_Z = 184$ , corresponding to  $W$ , with a charge  $Z_Z$  varying from 1 to 50 (full lines), for Ne  $A_Z = 20$  and  $Z_Z = 10$  (diamonds), for Ni  $A_Z = 56$  and  $Z_Z = 28$  (circles) and for Kr  $A_Z = 78$  and  $Z_Z = 36$  (squares).

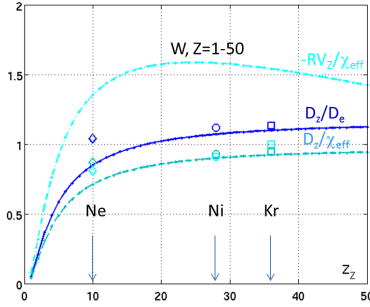


**Figure 13.** Ratio between the trace impurity diffusivity and  $1/\text{the electron diffusivity}$  (blue)  $2/\text{the effective heat diffusivity}$  (sky blue), ratio between the  $-R\times$  the trace impurity convective velocity (cyan) and the effective heat diffusivity versus  $Z_z$ , for the TEM1 case (see Table 1). For  $A_Z = 184$ , corresponding to  $W$ , with a charge  $Z_Z$  varying from 1 to 50 (full lines), for Ne  $A_Z = 20$  and  $Z_Z = 10$  (diamonds), for Ni  $A_Z = 56$  and  $Z_Z = 28$  (circles) and for Kr  $A_Z = 78$  and  $Z_Z = 36$  (squares).

ITG dominated regimes, the trace impurity convective contribution, directed inward, can be up to 6 times larger than the total effective diffusivity  $\chi_{eff}$ . This observation could explain the observed fast impurity transport in Laser Blow Off (LBO) experiments on ASDEX Upgrade [8, 9], Tore Supra and JET [10], and CMOD [?]. Simulations relevant for the interpretation of LBO experiments will be carried out in the following section dedicated to integrated modelling.

## 5. Integrated modelling with multiple-isotope transport

The implications of the trends explored in the previous sections are here illustrated through analysis of multiple-isotope transport dynamics within an integrated modelling framework. The transport code

applied for the simulations is JETTO [18, 19], with QuaLiKiz predicting the turbulent transport.

The starting point, for our thought numerical experiments, was the well studied JET shot #87412, previously analysed using JETTO+QuaLiKiz leading to good agreement with the experimental measurements [17]. A multiple-isotope scenario was then artificially imposed on the simulations by introducing a H species with  $n_H/n_D = 1$  in the  $\rho = 0.85 - 1.0$  region, where  $\rho$  is the normalised toroidal flux coordinate. The electron density profile  $n_e$  was kept as in the original discharge. Simulations with varying initial conditions were carried out, as described in the subsections below. For each case, the current and the toroidal momentum were interpretive, while electron temperature, ion temperature, H ion density and D ion density were predictive. No impurities, neutrals, or MHD (NTMs, sawteeth) were included. All NBI source calculations are from PENCIL. To simulate various regimes, the sources were artificially modified in the various cases, as described below. Neoclassical transport was calculated by NCLASS [32].

QuaLiKiz was applied in the region  $0.15 < \rho < 0.85$ . For the inner core at  $\rho < 0.15$ , where typically QuaLiKiz does not predict turbulent flux, the transport was prescribed to ensure smooth profiles towards the magnetic axis. For  $\rho > 0.85$  the profiles are prescribed from the measurements.

Simulations in two separate regimes were studied. The first was the nominal regime corresponding to the actual experimental conditions, starting with an initially peaked electron density profile. All ion-scale modes were ITG dominated modes. The second regime was a TEM dominated regime. Finally, an ITG dominated regime is studied starting from a hollow density profile, this situation being more representative of on edge/SOL fuelling case.

All simulations were run for 3 seconds of JET plasma evolution, with a stationary particle source, sufficient for all profiles to converge, the energy confinement being around 95 ms for the ITG case and 46 ms for the TEM case.

### 5.1. ITG dominated regime, $Q_i > Q_e$

First, in D only, a stationary state for  $T_i$ ,  $T_e$  and  $n_e$  was set by running JETTO+QuaLiKiz until full profile relaxation, with boundary conditions at  $\rho = 0.85$  determined from averaging the experimental profiles between 10.0-10.5 s. Then, a 50 - 50 concentration of H and D was imposed at the  $\rho = 0.85$  boundary condition. In the first simulation, the NBI particle source was imposed to be pure D, and the JETTO+QuaLiKiz simulation restarted until stationary state was reached once more. The relaxed profiles are seen in Fig. 14. Both H and D profiles are



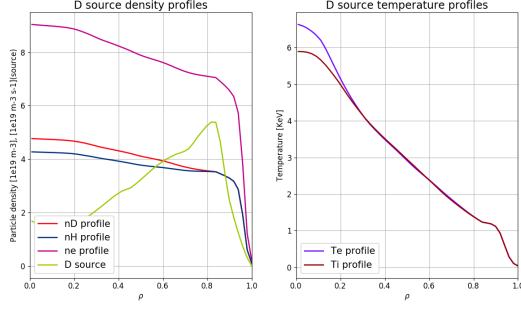


**Figure 14.** Relaxed density profiles for a D particle source (left panel) and ion and electron temperature profiles (right panel), for  $n_H = n_D$  at  $\rho = 0.85$ , at 13 s.

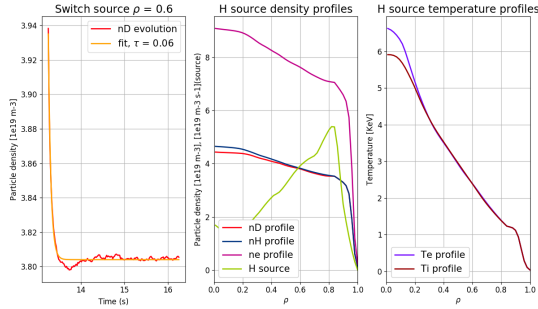


**Figure 15.** Evolution of the D density profile at  $\rho = 0.6$  following a switch of particle source from D to H (left panel). The  $\tau$  relaxation timescale is from an exponential fit. The central panel shows the final relaxed density profiles in presence of a H source, while the right panel shows the relaxed temperature profiles, at 16 s.

peaked, even though the particle source is on D only. Indicating that both D and H profiles are controlled rather by the electron density profile, the large  $D_i$  and an inward  $V_i$ , as expected from Turbulence Equipartition [33, 34]. Note that the NBI source is peaked off-axis due to the high density of this JET-ILW baseline discharge.

We then proceed to separate the ion and electron particle confinement timescales.

In the first case, the D particle source was switched to a H particle source. The H and D profiles evolved during the 3 s simulation time, while the electron density remains unchanged. The D profile evolution at  $\rho = 0.6$  can be seen in Fig 15 (left panel). The final density profiles for D, H and electrons are visible in Fig 15 (central panel), the final  $T_i$  and  $T_e$  (right panel) are similar to the initial ones Fig. 14. The D relaxation timescale was determined to be  $\tau = 0.06$  s following an exponential fit.

In the second case, all particle sources were turned off to identify the timescale of electron particle

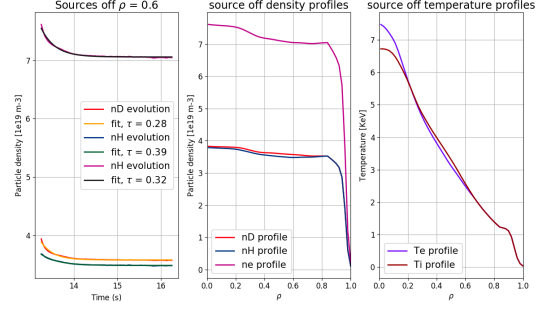


**Figure 16.** Evolution of  $n_e$  and  $n_D$  at  $\rho = 0.6$  after turning off all particle sources (left panel). The final relaxed density profiles are shown in the central panel, the final temperature profiles are shown in the right panel, at 16 s.

transport. The results are shown in Fig. 16, with the left panel corresponding to the decay of  $n_e$  and  $n_D$  at  $\rho = 0.6$ , and the final relaxed density profiles shown in the central panel, again on the right panel one sees that  $T_i$  and  $T_e$  remain unchanged throughout the simulation. The decay of D and  $n_e$  perfectly coincide, since the evolving electrons control the isotope transport. As expected from previous sections, this timescale is around 5 times slower than the isotope mixing case, with  $\tau = 0.28$  s, see table 4. It is also interesting to note that the final electron density profile, without source, is slightly flatter than the initial with a off-axis source.

### 5.2. TEM dominated regime, $Q_e \gg Q_i$

In a TEM dominated regime, the starting point was the pulse #87412, but with prescribed reduced density to reduce the collisionality and increase the TEM drive. Furthermore, the heating power was forced to only heat the electrons to obtain  $T_e \gg T_i$  and reach a TEM dominated regime. The same numerical experiments were carried out: exchanging the D particle source to a H source and switching off the particle source.

The final stationary states of the mixed-isotope simulation with a D particle source, are shown respectively in Fig. 17. It is striking that, in the TEM dominated case, as opposed to the ITG dominated case, there are significant differences in the isotope profiles. In Fig. 18, when exchanging the D source to a H source, we find an isotope remixing time of  $\tau \approx 0.35$  s, significantly slower than the analogous simulation in the ITG dominated case see table 4, due to lower  $D_i$  and  $V_i$  in the TEM dominated case.

When the particle source is removed, Fig. 19, the time scale needed for the D profile to relax to a new shape is  $\tau \approx 0.47$  s. This time is comparable to the isotope mixing time, see table 4. Moreover, we do not have significantly faster electron particle transport in the TEM dominated regime compared

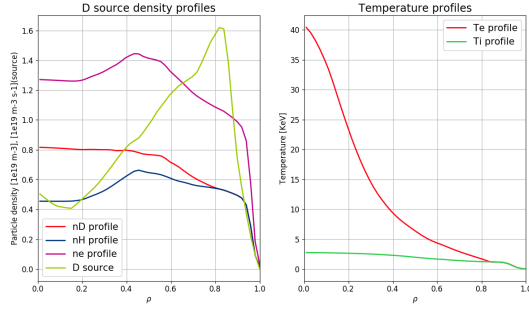


**Figure 17.** Simulation of a prescribed TEM dominated regime, with a D particle source and both H and D isotopes. The final states of the densities are shown in the left panel. The temperature profiles are shown in the right panel at 13 s.

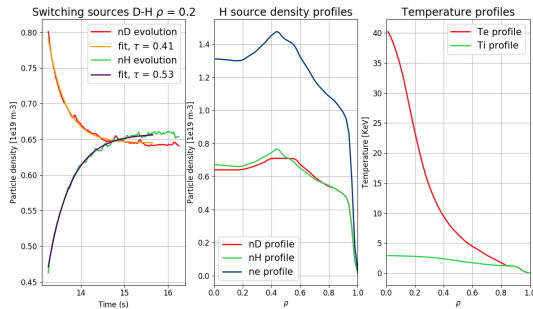


**Figure 18.** TEM dominated regime. Evolution of D and H density when exchanging the particle source from D to H (left panel), relaxed final densities in presence of a H source (central panel) and temperature profiles (right panel) at 16 s.

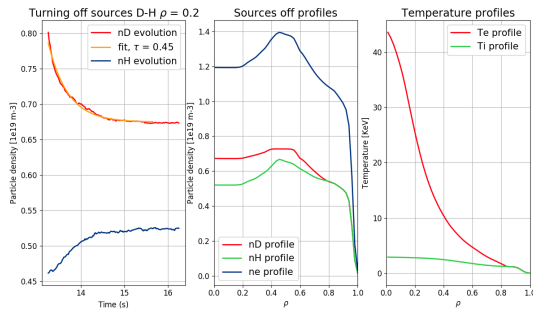


**Figure 19.** TEM dominated regime. Evolution of D and H density when turning off the particle source (left panel). Relaxed density (central panel) and temperature (right panel) profiles at 16 s.

to the ITG dominated regime. This is consistent with the analytical findings in section 3 showing that the passing ions can still provide significant transport in a TEM regime.

### 5.3. ITG dominated regime, $Q_i > Q_e$ . Hollow density profiles.

Of relevance to core fuelling is the timescale of isotope mixing starting from a hollow density profile, e.g. following a gas puff or pellet injection. To analyse this, the starting point is now the measured #87412 kinetic profiles at 9 s, corresponding to the time directly following the L to H transition where the initial  $n_e$  profile is hollow, see Fig. 20. To compare isotope and electron transport timescales two numerical experiments are carried out. First the hollow electron density profile evolves, with a D source and D only, until it reaches a stationary peaked state, see Fig. 20. The left plot displays the initial and final  $n_e$  profiles of the simulation, with the  $n_e$  evolution at  $\rho = 0.2$  shown in the right plot. The timescale for the filling in and relaxation of the  $n_e$  profile was  $\tau_e = 0.58$  s. Similar slow time scales were found JET high  $I_p$  of off-axis particle source experiments [35] and in the associated CRONOS-QuaLiKiz modelling [36].

In a second numerical experiment, a  $n_H$  profile with an initial hollow profile similar to the initial  $n_e$  illustrated on Fig. 20a was added to the system. The boundary condition at  $\rho = 0.85$  was set to  $n_H = n_D$ . The electron profile was left unchanged (the final profile from Fig. 20a), and the D profile was adjusted to match quasineutrality. The simulation was restarted, and the relaxation time of the system then corresponded to the H isotope relaxation time, evolving from hollow to peaked. The results are shown in figure 21. As expected, an evolution for the isotope mixing an order of magnitude faster than the electron hollow-to-peaked time was observed:  $\tau_H = 0.057$  s, see also table 5. Note that two timescales are evident in Fig. 21. The fast timescale of the major evolution of H, and then a slower timescale corresponding to the correction due to a minor evolution of  $n_e$  which then impacts the  $n_H$  profile as well.

## 6. Conclusion

Thanks to a comprehensive approach including nonlinear gyrokinetic modelling, analytical derivation, quasi-linear modelling and integrated source driven modelling, we have demonstrated that ion particle transport coefficients differ significantly from electron particle transport coefficients while respecting ambipolar fluxes.

In the case of dominant ITG turbulence (i.e.  $Q_i > Q_e/2$ ), ratios of the ion to electron diffusive and convective terms up to 5 are obtained. The resonance condition, in the case of ITG dominated turbulence, leads to both larger ion heat fluxes as well as larger ion particle diffusive and convective

Case	ITG dominated case		TEM dominated case	
	D relaxation time scale $\tau_D$ in ms	$\tau_D/\tau_E$	D relaxation time scale $\tau_D$ in ms	$\tau_D/\tau_E$
Switch sources	60	0.6	410	8.7
Turn off source	280	3.0	450	9.8

**Table 4.** Summary of the characteristic time scales for initially peaked density profiles and either ITG or TEM dominated regimes. "Switch sources" refers to the switching from a D source to an H particle source. "Turn off source" refers to turning off the particle source, while keeping the heating source.

Case	D(e)	D(H)	D(D)	Vc(e)	Vc(H)	Vc(D)	Vt(e)	Vt(H)	Vt(D)
ITG switching sources	0.15	1.36	1.28	0.16	-1.33	-1.23	-0.093	0.99	0.73
ITG source off	0.37	2.60	2.31	0.41	-2.73	-2.41	-0.31	2.78	2.20
TEM switching sources	1.92	0.62	0.48	-1.45	0.33	0.12	0.71	-0.26	-0.27
TEM source off	2.98	0.94	0.67	-2.93	0.33	0.85	1.95	-0.39	-0.38
Hollow H profile	0.18	1.57	1.38	0.19	-1.51	-1.32	0.16	1.28	0.98
Hollow He profile	0.17	1.24	1.59	0.14	-2.13	-1.36	-0.91	1.15	0.93

**Table 5.** Summary of the particle transport coefficients for the various cases at  $\rho = 0.6$ . D(e), D(H) and D(D) are the diffusion coefficients, in  $m^2/s$ , for electrons, Hydrogen and Deuterium. Vc and Vt are the pure convective term and the thermodiffusion term, in m/s

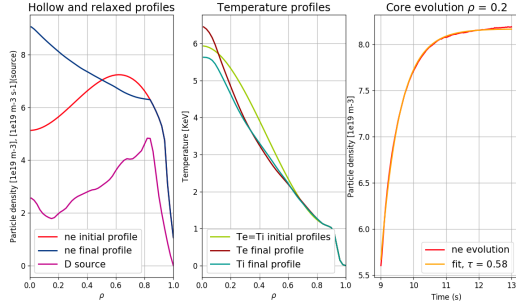


**Figure 20.** Simulation starting from the #87412 profiles following the L to H transition. The electron density initial and final profiles for the hollow-to-peaked transition are shown in the left panel, the particle source profile is also displayed. The central panel shows the initial and final temperature profiles. The  $n_e$  (and thus  $n_D$ ) evolution at  $\rho = 0.2$  is shown in the right panel.

coefficients. This dependence of  $D_i/D_e$  on the resonance condition is strongly related to the well known result that ion heat flux dominates electron heat flux for ITG dominated regimes, and electron heat flux is dominant for TEM regimes. In the present work on the particle flux ratio, the results are obtained in nonlinear gyrokinetic simulations using GKW [15], are derived in the quasilinear analytical limit, and confirmed with QuaLiKiz [24] where the quasilinear particle diffusivities are very close to the nonlinear results for both ITG and TEM dominated cases. Moreover, in JETTO-QuaLiKiz [?] source driven numerical experiments, similar H and D density profiles are obtained independently of the nature of the ion core particle source (i.e. either H or D), with a isotope mixing time much shorter than the electron

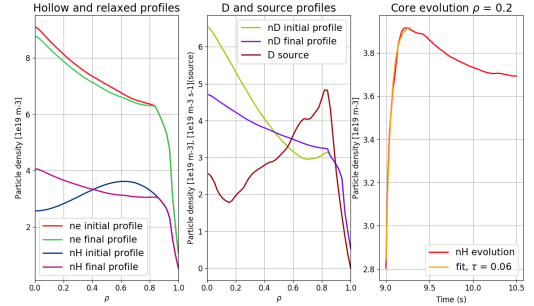


**Figure 21.** Simulation starting as in figure 20, with the addition of a hollow isotope (H) profile, to isolate the isotope filling-in time. In the left panel, the initial  $n_e$  profile is shown in red, and the final  $n_e$  profile in green. Initial and final  $n_H$  profiles are shown in blue and purple. A boundary condition of  $n_H = n_D$  was set at  $\rho = 0.85$ . The central panel shows the D particle source in red, as well as the initial (gold) and final (purple)  $n_D$  profiles. There was no H particle source in the simulation. The time evolution and fitted relaxation timescale of  $n_H$  at  $\rho = 0.2$  is shown in the right panel.

particle transport time. The situation reverses in the case of TEM dominated turbulence (i.e.  $Q_e > 2 \times Q_i$ ), where  $D_i < D_e$  and  $V_i < V_e$  are obtained and where the ion mixing time is of the same order of the electron particle transport time.

In tokamaks, in presence of sufficient ion heating such that  $Q_i > Q_e/2$ , dominant ITG regime is often encountered.  $Q_i > Q_e/2$  is also expected in reactor-relevant high density plasmas where the ion-electron heat exchange and radiation contributions plays a significant role [37]. And indeed, it is interesting to note that our findings are in agreement with numerous experimental observations: similar H and D density



profiles in JET-ILW in presence of core D source [4], very fast trace T transport in TFTR [1], similarly for trace He in DIII-D plasmas [5], laser blow off of impurities showing impurity transport times significantly larger than the energy confinement time [38] and references therein.

The next step is to model existing and future isotope DT experiments in JET and past laser blow off experiments using QuaLiKiz-JETTO. ITER scenarios will then be addressed focusing on isotope mixing, He ash transport, edge fuelling, impurity contamination in H, He and DT scenarios thanks to JETTO-QuaLiKiz.

## Acknowledgments

The authors are grateful for discussions with S. Breton, N. Dubuit, E. Fable, X. Garbet, L. Garzotti, R. Guirlet, E. Militello-Asp, M. Romanelli, M. Schneider. The work has been carried out within the framework of the EUROfusion Consortium and has received funding from the Euratom research and training programme 2014-2018 under grant agreement No 633053. The views and opinions expressed herein do not necessarily reflect those of the European Commission. The authors acknowledge access to the EUROfusion High Performance Computer (Marconi-Fusion) through EUROfusion and to the HPC resources of Aix-Marseille Université financed by the project Equip@Meso (ANR-10-EQPX-29-01).

- [1] P. C. Efthimion, L. C. Johnson, J. D. Strachan, E.J. Synakowski, M. Zarnstorff, H. Adler, C. Barnes, R. V. Budny, F.C. Jobs, M. Loughlin, D. McCune, D. Mueller, A. T. Ramsey, G. Rewoldt, A. L. Roquemore, W. M. Tang, and G. Taylor. Tritium particle transport experiments on tftr during d-t operation. *Physical Review Letters*, 75(1), 1995.
- [2] K-D Zastrow *et al.* 2004 *Plasma Phys. Control. Fusion* 46 B255.
- [3] M. Valovic *et al.* *ITPA Transport and Confinement, May 2017, Princeton*, 2017.
- [4] M. Maslov *et al.*, to be submitted to Nucl. Fusion.
- [5] M. R. Wade, D. L. Hillis, J. T. Hogan, R. Maingi, M. M. Menon, M. A. Mahdavi, W. P. West, K. H. Burrell, P. Gohil, R. J. Groebner, R.M. Hong, D. H. Kellman, J. C. Phillips, R. P. Seraydarian, the DIII-D Team, and D. F. Finkenthal. Helium transport and exhaust studies in enhanced confinement regimes in diiD. *Physics of Plasmas*, 2(6):2357–2365, 1995.
- [6] C. Angioni *et al.*, Nucl. Fusion 49 055013 (2009).
- [7] C. Estrada-Mila, J. Candy, and R. E. Waltz. Gyrokinetic simulations of ion and impurity transport. *Physics of Plasmas*, 12(2):022305, 2005.
- [8] R. Dux *et al.*, Plasma Phys. Control. Fusion 45, 1815-1825 (2003).
- [9] C. Angioni *et al.*, Plasma Phys. Control. Fusion 49 2027 (2007).
- [10] M. Mattioli *et al.*, Nucl. Fusion 35 1115 (1995).
- [11] C. Angioni and A. G. Peeters Phys. Rev. Lett. 96 095003 (2006).
- [12] C. Angioni *et al.* 2007 *Phys. Plasmas* 14 055905.
- [13] F.J. Casson, R.M. McDermott, C. Angioni, Y. Camenen, R. Dux, E. Fable, R. Fischer, B. Geiger, P. Manas, L. Menchero, G. Tardini, and the ASDEX Upgrade Team. Validation of gyrokinetic modelling of light impurity transport including rotation in asdex upgrade. *Nuclear Fusion*, 53(6):063026, 2013.
- [14] C Angioni *et al.* 2015 *Phys. Plasmas* 22 055902.
- [15] A. G. Peeters, Y. Camenen, F. J. Casson, W. A. Hornsby, A. P. Snodin, D. Strintzi, and G. Szepesi. The nonlinear gyro-kinetic flux tube code GKW. *Computer Physics Communications*, 180(12):2650–2672, 2009.
- [16] C. Bourdelle, X. Garbet, F. Imbeaux, A. Casati, N. Dubuit, R. Guirlet, and T. Parisot. A new gyrokinetic quasilinear transport model applied to particle transport in tokamak plasmas. *Physics of Plasmas*, 14(11):112501, 2007.
- [17] Tractable flux-driven temperature, density, and rotation profile evolution with the quasilinear gyrokinetic transport model qualikiz. *Plasma Phys. Control. Fusion*, 59(12):124005, 2017.
- [18] G. Cenacchi, A. Taroni, JETTO: A free-boundary plasma transport code, JET-IR (1988).
- [19] M. Romanelli *et al.* 2014 *Plasma and Fusion Research* Volume 9, 3403023.
- [20] R.E. Waltz, G. D. Kerbel, and J. Milovich. *Phys. Plasmas*, 1:2229, 1994.
- [21] R. L. Miller, M. S. Chu, J. M. Greene, Y. R. Lin-Liu, and R. E. Waltz. Noncircular, finite aspect ratio, local equilibrium model. *Physics of Plasmas (1994-present)*, 5(4):973–978, 1998.
- [22] C Bourdelle, X Garbet, F Imbeaux, A Casati, N Dubuit, R Guirlet, and T Parisot. A new gyrokinetic quasilinear transport model applied to particle transport in tokamak plasmas. *Physics of Plasmas*, 14(11), 2007.
- [23] A. Casati, C. Bourdelle, X. Garbet, F. Imbeaux, J. Candy, F. Clairet, G. Dif-Pradalier, G. Falchetto, T. Gerbaud, V. Grandgirard, Oe D. Guercan, P. Hennequin, J. Kinsey, M. Ottaviani, R. Sabot, Y. Sarazin, L. Vermare, and R. E. Waltz. Validating a quasi-linear transport model versus nonlinear simulations. *Nuclear Fusion*, 49(8):085012, 2009.
- [24] C Bourdelle, J Citrin, B Baiocchi, A Casati, P Cottier, X Garbet, F Imbeaux, and JET Contributors. *Plasma Physics and Controlled Fusion*, 58:014036, 2016.
- [25] J. Citrin, C. Bourdelle, P. Cottier, D. F. Escande, Oe D. Guercan, D. R. Hatch, G. M. D. Hogewijf, F. Jenko, and M. J. Pueschel. Quasilinear transport modelling at low magnetic shear. *Physics of Plasmas*, 19(6), JUN 2012.
- [26] P Cottier, C Bourdelle, Y Camenen, Ö D Gürcan, F J Casson, X Garbet, P Hennequin, and T Tala. Angular momentum transport modeling: achievements of a gyrokinetic quasi-linear approach. *Plasma Physics and Controlled Fusion*, 56(1):015011, 2014.
- [27] C. Bourdelle. Turbulent transport in tokamak plasmas: bridging theory and experiment. *Habilitation à Diriger des Recherches, Aix-Marseille University*, 2015.
- [28] C Angioni, E Fable, M Greenwald, M Maslov, A G Peeters, H Takenaga, and H Weisen. Particle transport in tokamak plasmas, theory and experiment. *Plasma Physics and Controlled Fusion*, 51(0):124017, 2009.
- [29] C. Angioni, Y. Camenen, F.J. Casson, E. Fable, R.M. McDermott, a.G. Peeters, and J.E. Rice. Off-diagonal particle and toroidal momentum transport: a survey of experimental, theoretical and modelling aspects. *Nuclear Fusion*, 52(11):114003, November 2012.
- [30] E. Fable *et al.*, 2017 *Nucl. Fusion* 57 022015, and private communication.
- [31] J.Y. Kim and H.S. Han 2017 *Phys. Plasmas* 24 072501.
- [32] W.A. Houlberg, K.C. Shaing, S.P. Hirshman and M.C. Zarnstorf, 1997 *Phys. Plasmas* 4 3230.
- [33] J. Nycander and V. V. Yankov. Anomalous pinch flux in tokamaks driven by the longitudinal adiabatic invariant.

- Physics of Plasmas (1994-present)*, 2(8):2874–2876, 1995.
- [34] V. Naulin, J. Nycander, and J. Juul Rasmussen. Equipartition and transport in two-dimensional electrostatic turbulence. *Phys. Rev. Lett.*, 81:4148–4151, Nov 1998.
  - [35] A. Loarte, M.J. Leyland, J.A. Mier, M.N.A. Beurskens, I. Nunes, V. Parail, P.J. Lomas, G.R. Saibene, R.I.A. Sartori, L. Frassinetti, and JET EFDA Contributors. Plasma density and temperature evolution following the h-mode transition at jet and implications for iter. *Nuclear Fusion*, 53(8):083031, 2013.
  - [36] Baiocchi B., Bourdelle C., Angioni C., Imbeaux F., Loarte A., Maslov M., and JET EFDA contributors. Transport analysis and modelling of the evolution of hollow density profiles plasmas in jet and implication for iter. *To be published in Nuclear Fusion*, 2015.
  - [37] E. Fable, R. Wenninger, and R. Kemp. Selected transport studies of a tokamak-based demo fusion reactor. *Nuclear Fusion*, 57(2):022015, 2017.
  - [38] M. Mattioli, R. Giannella, R. Myrnas, C. Demichelis, B. Denne-Hinnov, T. Dudok De Wit, and G. Magyar. Laser blow-off injected impurity particle confinement times in jet and tore supra. *Nuclear Fusion*, 35(9):1115, 1995.